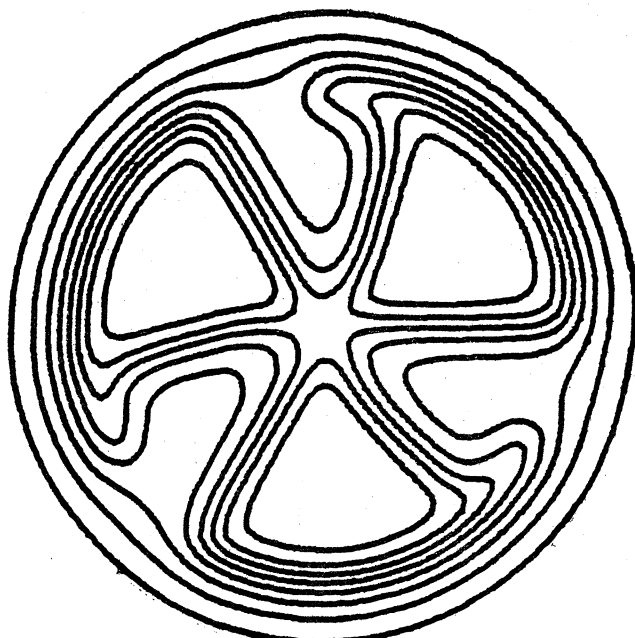


MICHIGAN STATE UNIVERSITY  
CYCLOTRON LABORATORY

PREEQUILIBRIUM ANALYSIS OF ( $p, n$ ) SPECTRA ON VARIOUS TARGETS  
AT PROTON ENERGIES OF 25 TO 45 MeV

M. BLANN, R. R. DOERING, AARON GALONSKY, D. M. PATTERSON,  
and F. E. SERR



PREEQUILIBRIUM ANALYSIS OF (p,n) SPECTRA ON VARIOUS TARGETS  
AT PROTON ENERGIES OF 25 TO 45 MeV\*

PREEQUILIBRIUM ANALYSES OF (p,n) REACTIONS

M. Blann  
Nuclear Structure Research Laboratory and Dept. of Chemistry  
University of Rochester and Physics Department  
R.R. Doering, Aaron Galonsky, D.M. Patterson and F.E. Serr††  
Cyclotron Laboratory and Physics Department  
Michigan State University  
Rochester, New York 14627  
and  
East Lansing, Michigan 48824

**ABSTRACT:** Thin target (p,n) spectra are reported for incident proton energies of 25, 35 and 45 Mev on  $^{48}\text{Ca}$ ,  $^{90}\text{Zr}$  and  $^{120}\text{Sn}$ , and at proton energies of 35 and 45 Mev on  $^{208}\text{Pb}$ . Angle-integrated spectra are compared with predictions of the geometry-dependent hybrid model, the hybrid model, and hybrid model with average state lifetimes.<sup>1</sup> The geometry-dependent hybrid model, when combined with evaporation components, gives an excellent prediction of the overall shapes and magnitudes of the experimental results. The simpler hybrid model fails in both respects, paralleling results of earlier comparisons of (p,p') spectra with model calculations.

NUCLEAR REACTIONS  $^{48}\text{Ca}$ ,  $^{90}\text{Zr}$ ,  $^{120}\text{Sn}$ ,  $^{208}\text{Pb}$  (p,n);  
E=25, 35, 45 MeV; measured  $\sigma(\text{En}, \theta)$  and  $f_{\text{diss}}(\text{En}, \theta)$ ;  
enriched targets.

1. Introduction  
The high-energy components of many particle spectra have been successfully interpreted in terms of preequilibrium decay models.<sup>1</sup> The model which has had broadest application and greatest success is the hybrid/geometry dependent hybrid (GDH) model. These formulations have had success in reproducing many ( $\alpha$ ,p), ( $\alpha$ ,n), ( $^3\text{He}$ ,p), and ( $p$ ,p') spectra. Agreement has been found for a broad range of target masses and bombarding energies.

Relatively few comparisons have been performed for (p,n) spectra. Grimes et al. have applied the GDH model to the  $^{51}\text{V}$ (p,n) reaction at proton energies between 16 and 26 MeV, with quite satisfactory results.<sup>2</sup> Agreement at higher energies remains to be demonstrated. Indeed it has been suggested that the model will predict incorrect spectral shapes and yields for (p,n) reactions, and that the good agreement found in reproducing (p,p') spectra is fortuitous.<sup>3</sup> This work is addressed to investigating the applicability of the geometry-dependent hybrid model to the a-priori calculation of (p,n) spectra on targets from  $^{48}\text{Ca}$  to  $^{208}\text{Pb}$ , for proton energies of 25 to 45 Mev.

Experimental measurements of (p,n) spectra on  $^{48}\text{Ca}$ ,  $^{90}\text{Zr}$ ,  $^{120}\text{Sn}$  and  $^{208}\text{Pb}$  will be presented and described in section 2. The physical principles of the formulation to be applied in interpretation of these data will be sketched in section 3, with finer details of parameter evaluation

\* Work supported partially by the National Science Foundation,  
U.S. Energy Research and Development Administration and the  
Office of Naval Research.

† Present address: University of Texas, Austin, Texas 78712

†† Present address: Stanford University, Stanford, CA 94305

referred to earlier works. The GDH model results will then be compared with experimental spectra in section 4, to partially answer the questions raised above.

## 2. Experimental Technique

The Michigan State University cyclotron provided 25-, 35-, and 45-MeV proton beams for bombarding  $^{48}\text{Ca}$ ,  $^{90}\text{Zr}$ ,  $^{120}\text{Sn}$ , and  $^{208}\text{Pb}$  targets with isotopic enrichments of 96.25, 98.66, 98.40 and 99.14%, respectively. Their thicknesses were approximately 10 mg/cm<sup>2</sup>, except for the 1 mg/cm<sup>2</sup>  $^{48}\text{Ca}$  target and a pair of 30 mg/cm<sup>2</sup>  $^{208}\text{Pb}$  targets used at 35 and 45 MeV.

Neutrons and gamma rays from these targets were detected with a 7.0-cm-diameter by 3.8-cm-thick NE213 scintillator coupled to an RCA 8575 photomultiplier (PM) tube. Time-of-flight (TOF) spectra were obtained by starting a time-to-amplitude converter (TAC) with a constant-fraction-of-pulse-height trigger (CFPHT) on the PM anode current and stopping the TAC with a zero-crossing discriminator (ZCD) on the cyclotron RF voltage. Another TAC was started with a ZCD on the doubly-differentiated PM ninth-dynode signal and stopped with a delayed output from the CFPHT. This provided a pulse-shape-discrimination<sup>4</sup> (PSD) signal which, together with the singly-differentiated PM ninth-dynode (LIGHT) signal, enabled the events to be identified in terms of the particle producing the scintillation. Digital gates set around the proton and electron bands in the LIGHT-PSD plane defined

neutron- and gamma-ray-induced events corresponding primarily to n-p and Compton scattering, respectively, in the scintillator.

Figures 1a-d display the neutron and gamma-ray TOF spectra from all four targets at a scattering angle of 10° and a beam energy of 45 MeV. Similar spectra have been acquired at 0° and in 5° steps out to 160° for all three beam energies. Each channel corresponds to 0.1 nsec, and TOF decreases with increasing channel number. Thus, higher-energy neutrons appear to the right. The prominent peak in each gamma-ray spectrum results from the 50.5 nsec (FWHM) beam bursts incident on the target and demonstrates the intrinsic time resolution of the system. A measure of the PSD is provided by the 'leakage' of the target gamma-ray peak into the neutron spectrum, which is usually between 1/28 and 2%. The most prominent peak in each neutron spectrum is the isobaric analog of the target ground state (IAS).

The IAS peaks are somewhat broader than the target gamma-ray peaks, due principally to the scintillator thickness and to beam energy loss in the target. For the IAS of  $^{208}\text{Pb}$ , the intrinsic width of the state ( $\Gamma=231\pm 6$  keV)<sup>5</sup> is also significant. The neutron energy resolution is proportional to  $\epsilon_h^{3/2}$  (nonrelativistically) and is about 1-1/2 MeV for our most energetic neutrons ( $\epsilon_n \approx 45$  MeV).

The dynamic ranges of the TOF spectra are limited by the cyclotron RF period, which is 51 nsec for  $E_p = 45$  MeV. The TOF TAC stop signals have been delayed so that the maximum-

energy neutrons from each reaction arrive at some channel between 450 and 500 in figs. 1a-d. The same channels contain a few much-lower-energy neutrons from the previous beam burst which took 51 nsec longer to traverse the 4.25-m flight path. Such overlap has been greatly suppressed by setting sufficiently high thresholds on the light signals to give very little detection efficiency for these low-energy neutrons. Thus, increasing numbers of neutrons from the previous beam burst fill the channels just above the highest-energy neutrons in each TOF spectrum until they are cut off by the maximum interval between start and stop signals (the RF period). The TOF spectra are terminated at low channel numbers by the nonlinearity of the initial part of the TAC range.

Since the principal reason for taking these data was to obtain accurate ( $p, n$ )-IAS differential cross sections<sup>6)</sup>, the experimental setup was not always optimum for measuring the cross sections for producing neutrons of other energies. In particular, dynamic range was generally sacrificed for neutron energy resolution. For  $^{208}\text{Pb}$  at  $E_p = 25 \text{ MeV}$ , the data span such a limited dynamic range that they have not been included in the present study.

Occasional measurements with a "shadow bar" interposed between the target and the detector indicate that typically 10% of the observed neutrons originate outside the target. The background from such extraneous sources has been minimized by heavily shielding the beam dump and the detector.

Figures 1e-h display the neutron spectra of figs. 1a-d

after conversion from counts per time interval to differential cross section per MeV of neutron energy in the laboratory coordinate system. The bin width is 100 keV. The cross sections have an estimated accuracy of about  $\pm 20\%$ . Most of the error results from uncertainties in the background. In each case where a target gamma-ray peak is noticeable in the neutron TOF spectrum, the gamma-ray spectrum has been multiplied by the ratio of target gamma-ray counts in the two spectra and subtracted from the neutron spectrum. The low-energy overlap has been extrapolated under the high-energy end of each neutron spectrum down to an estimated constant background of non-target neutrons, which has also been subtracted. The 20% error estimate also includes 10% uncertainties in the neutron detection efficiencies calculated with a modified version of Kurz's code<sup>7)</sup> and 5% contributions from the measurements of target thickness and the calculations of neutron attenuation along the flight path.

More detailed descriptions of the MSU neutron TOF system and the calculations of detector efficiency and neutron attenuation are available in refs. 6, 8 and 9. For comparison with calculated results, the measured differential cross sections have been angle-integrated to yield the cross sections per MeV, which are displayed in figures 4-11 and discussed in section 4.

### 3. Preequilibrium decay models

Many spectra [e.g.,  $(a,p)$ ,  $(p,p')$ ,  $(p,n)$ , etc.] have shown high-energy components in the continuum which were not explicable by compound-nucleus decay theory nor by direct-reaction models. These spectral components have been analyzed by models called preequilibrium, or precompound-decay models, which attempt to interpret these components as due to particle emission of the equilibrating system.

Several of the models which have been most widely used are dependent in their formulation on the use of partial state densities with a statistical assumption, which follows from the work of Griffin.<sup>10</sup> In these models, the equilibration process is viewed as occurring through successive two-body interactions, such that, e.g., for a nucleon-induced reaction one starts with a two particle-one hole excited state ( $2p1h$ ) following the first projectile-target interaction, proceeding through a hierarchy of more complicated states ( $3p2h$ ,  $4p3h$ , etc.) until an equilibrium distribution is achieved. The probability or cross section for particle emission during this process is obviously dependent on the probability that the particle will be found in the required energy range during the equilibration period; more precisely the emission cross section must be equal to the product of the number of particles to be found in the required energy range and ratio of emission width to total width.

The determination of the number of particles in a given energy range has, as stated, been provided by means of state densities determined by the number of excited particles and holes ( $p,h$ ); or excitons,  $n$  ( $n=p+h$ ). The formula generally used is one due to Ericsson; with energy  $E$  and single particle state density  $g$ , it is

$$\rho_{p,h}(E) = \rho_n(E) = \frac{g(gE)^{n-1}}{p!h!(n-1)!} \quad (1)$$

with the assumption that every state of a given heirarchy ( $n$ ) is populated with equal a-priori probability during the equilibration process. This seems to imply a statistical or quasi-equilibrium assumption, which should be looked at more closely.

If models as described in this section are to lead to equilibrium distributions in particle and hole number, it is necessary that the transition rate to higher  $n$  values ( $\lambda_+$ ) be greater than the reverse values ( $\lambda_-$ ), i.e.  $\lambda_+ > \lambda_-$  if  $n < \bar{n}$ , where  $\bar{n}$  is the most probable exciton number in the equilibrium distribution over  $n$ . If the statistical or quasi-equilibrium assumption is to be valid, it is required further that the transition (rearrangement) rate within a given heirarchy of states

$(\lambda_o)$  be greater than the transition rate to more complex states,  $\lambda_o > \lambda_+$ . It should be obvious that in fact  $\lambda_o \ll \lambda_+$ , since for the simple states important to precompound decay there are very few excited particles, but of the order of 50-200 nucleons below the Fermi energy. The transition rates should vary accordingly. If such an intuitive statement should not be obvious, actual estimates of these rates may be compared. Williams has applied the Golden rule using the average number of accessible final states based on eq. (1) to get relative rates<sup>12</sup>:

$$\begin{aligned}\lambda_+ &= \frac{2\pi}{N} |M|^2 \frac{g^2 E^2}{n+1} \\ \lambda_- &= \frac{2\pi}{N} |M|^2 g \cdot p \cdot h(n-2) \\ \lambda_o &= \frac{2\pi}{N} |M|^2 g^2 E \left(\frac{3n-2}{4}\right),\end{aligned}\quad (2)$$

where  $|M|^2$  is the average square of the two-body transition matrix, assumed constant and equal for the three processes of eq. (2). The single-particle level density for a Fermi gas is given by A/14. Taking the ratios of rates from (2) assuming  $p=h=\frac{n}{2}$  gives

$$\lambda_+/\lambda_- \approx 4(g_E^2)/(n+1)(n-2) \approx 4g_E^2/n^4 \quad (3)$$

$$\text{and } \lambda_+/\lambda_o \approx 4g_E/3n^2. \quad (4)$$

If one considers an example of the 2ph state of a mass 100 nucleus at 20 Mev of excitation, (3) gives  $\lambda_+/\lambda_- \approx 1000$ ; the condition for going toward  $\bar{n}$  is fulfilled. Equation (4) however gives  $\lambda_+/\lambda_o \approx 20$ , but the quasi-equilibrium requirement is that  $\lambda_+/\lambda_o \ll 1$ . Obviously, this condition is not fulfilled at excitations at which pre compound phenomena are observed.

Clearly, formulations based on the assumption of quasi-equilibrium at each stage of the equilibration process would appear to be established on erroneous assumptions. Yet such models have had extremely broad successes in reproducing experimental yields. There is a simple explanation for this. If one looks at a derivation of eq. (1), it is clear that a successive partition of energy between particles and holes is employed with the assumption that each partition has equal weighting (see the derivation in ref.13). If one looks at the kinematics for nucleon-nucleon scattering, it is seen that to first order, every allowed energy partition occurs with equal weighting after averaging over all initial and final collision angles<sup>13,14</sup>. The kinematics of the two-body scattering process therefore leads to an energy distribution between particles and holes as given by (1), quite independent of  $\lambda_+/\lambda_o$  values.

Use of (1) in these models amounts then to a closed-form

intranuclear-cascade calculation<sup>15</sup>, in which information of angular and geometric nature is not retained.

Having made these general comments on the physical basis of the model, we present the formulations to be used in this work, based on the hybrid model<sup>16</sup>. In this approach the differential cross section (mb/Mev) is given by

$$\begin{aligned} \frac{d\sigma}{d\epsilon} &= \sigma_R \sum_{n=n_0}^{\bar{n}} \left[ \frac{p_{n-1}(U)}{p_n(E)} g \right] \frac{\lambda_c(\epsilon)}{\lambda_c(\epsilon) + \lambda_+(\epsilon)} D_n \\ &= \sigma_R \sum_{n=n_0}^{\bar{n}} P_n(\epsilon), \end{aligned} \quad (5)$$

where  $\sigma_R$  is the total reaction cross section (mb), the quantity in the first set of brackets uses the partial state densities of eq.(1) to give particle populations in each energy interval, the quantity in the second set of brackets represents the emission to total width ratio, and  $D_n$  represents the population surviving prior particle emission. The sum is taken from the initial state,  $n=n_0$ , to the most probable value  $\bar{n}$ , with  $n$  changing by two units at each step, reflecting the particle-hole creation process due to the binary interactions assumed. The emission rate into the continuum for a particle at energy  $\epsilon$  is given by

$$\lambda_c(\epsilon) = \frac{\sigma \epsilon}{gV} \rho_c(\epsilon), \quad (6)$$

where  $\sigma$  is the inverse cross section,  $V$  the laboratory volume, and  $\rho_c(\epsilon)$  the density of states of the particle in the continuum. The intranuclear transition rate  $\lambda_+(\epsilon)$  has been evaluated in this model using either free nucleon-nucleon scattering cross sections corrected for the Pauli principle in nuclear matter, or using the imaginary optical potential<sup>17</sup> with parameters due to Bechetti and Greenlees,<sup>18</sup>

$$\lambda_+(\epsilon) = 2W/\hbar. \quad (7)$$

A more detailed discussion of the evaluation of parameters may be found in ref. 17.

Early analyses of  $(p,p')$  and  $(p,n)$  reactions suggested that a major contribution of the particle spectrum resulted from surface reactions.<sup>19,20</sup> The model was therefore reformulated to reflect contributions of different-density regions<sup>21</sup> as determined by the paths of each incident partial wave,

$$\frac{d\sigma}{d\epsilon} = \pi \bar{x}^2 \sum_{k=0}^{\infty} \sum_{n=n_0}^{\bar{n}} T_k \sum_{n=n_0}^{\bar{n}} P_n(\epsilon), \quad (8)$$

where  $T_k$  is the transmission coefficient for the incident particle, and where the parameters of  $P_n(\epsilon)$  were evaluated in a local-density approximation as described in ref. 17. In evaluating  $\lambda_+(\epsilon)$  according to the trajectory of the incident particle, two different (limiting) approximations are available options in the precompound-decay code. The first of these uses the maximum density or imaginary potential depth along the projectile path. This should

give an upper limit to  $\lambda_+(\epsilon)$  and, therefore, a lower limit to predicted particle spectra [since  $\lambda_+(\epsilon)$  appears in the denominator of (5)]. The second option provides an attempt to use an average value of the density or absorptive optical potential along the particle trajectory. To do this the density (potential) is averaged arbitrarily over a distance of five times the appropriate diffuseness parameter to the maximum density region. Since the density (potential) is approximately 1/150 of the saturation density at  $5a_0$ , this is thought to give a reasonable lower limit to  $\lambda_+(\epsilon)$  and, therefore, an upper limit to the predicted particle spectra. Since spectra calculated with these two limiting cases agree to well within a factor of two, no attempt has been made to define the average density (potential) more precisely; it is felt that the models should have an inherent uncertainty in predicted absolute cross sections of the order of a factor of two.

The calculations of this work employ two minor changes over earlier formulations, both involving the single-particle level-density parameter  $g$ . In earlier works  $g$  was kept constant as a function of excitation energy. In the calculations of this work, the  $g$  in eq. (4) was given an energy dependence characteristic of a Fermi gas,  $g(\epsilon)\epsilon^{1/2}$ , such that the Fermi-gas value ( $g=A/14$ ) was realized at the Fermi energy. The parameter  $g(\epsilon)$  was not given additional variation due to local-density approximations. Application of these changes to  $(p,p')$  spectra gave improved agreement with experimental results with respect to earlier calculations.

Results of such calculations are shown in figs. 2 and 3. In this work we make comparisons with  $(p,n)$  spectra.

Comparisons of results of eq. (5) using  $\lambda_+(\epsilon)$  calculated with nucleon-nucleon scattering cross sections, but with no geometry dependence, will also be presented in section 4 in order to illustrate the failure of the calculation when surface interactions are not included explicitly. Some precompound calculations have been performed using a formulation similar to eq. (5), but with the average lifetime of an n-exciton state,  $\langle\lambda_+(E)\rangle$ , rather than the lifetime of a particle at energy  $\epsilon$ ,  $\lambda_+(\epsilon)$ , in the emission-versus-transition-rate term.<sup>22</sup> It was found that when this was done, the intranuclear transition rate had to be decreased by factors of .3 to .2 in order to reproduce experimental excitation function yields.<sup>22</sup> It has been suggested that this adjustment is due to improper inclusion of spectator transitions in the overall bookkeeping of eq. (5) if  $\langle\lambda_+(E)\rangle$  is used in place of  $\lambda_+(\epsilon)$ .<sup>23</sup> Nonetheless, we have also included

results of eq. (5) with  $\langle\lambda_+(\epsilon)\rangle$  based on nucleon-nucleon scattering cross sections, with theoretical transition rates decreased by a factor of .25 in results to be presented in section 4.

#### 4. Results and Discussion

Geometry-dependent hybrid-model calculations which are presented in figs. 4-7 include results of eq. (6) for the first target-projectile interaction (a direct-reaction contribution). Higher-order contributions in particle-hole number were computed with eq. (3). Second-chance-emission contributions (two successive particles emitted prior to equilibrium) were computed for reactions at 45 MeV incident proton energy. This gave only a small contribution to the spectra, as is indicated in figs. 4-7.

The equilibrium evaporation code ALICE was used to generate compound-nucleus contributions of multiple neutron evaporation. Contributions due to  $^{48}\text{Ca}$  targets are shown in fig. 4; for other targets the evaporation contributions will be lower than the corresponding results for  $^{48}\text{Ca}$  at high neutron energies. This follows from the observation that higher mass targets will have a lower temperature at corresponding excitations. Curves representing the total calculated spectra are almost entirely due to the pre-equilibrium contributions, as it may be seen in fig. 4 that evaporation yields make significant contributions only at the lower neutron energies.

Results shown in figs. 4-7 used  $\lambda_+(\epsilon)$  values based on both the imaginary optical potential<sup>18</sup> and on the use of nucleon-nucleon scattering cross sections. Results of averaging the density by the two different options described

in Section 3 are illustrated in figs. 4-7. For 25-MeV incident protons, results based on both nucleon-nucleon scattering and on the imaginary optical potential give virtually identical results; at higher energies the results based on the imaginary optical potential differ somewhat from results based on N-N scattering. Both results should be considered as giving excellent agreement for an a-priori calculation of this type. Deviations between calculated and experimental results are not large relative to the 20% experimental uncertainties. Since an equidistant spacing approximation is explicit in eq. (1), these calculations can only give smooth spectra as results. If the experimental measurements at low residual excitations were made with poorer resolution, the apparent agreement with calculated results would be still better. The failure of some calculated results to give zero cross sections at the apparent ground state may be attributed to the experimental energy resolution giving experimental spectra beyond the known ground state. It may be seen in figs. 2-7 that no calculated results for (p,p') or (p,n) reactions are off by as much as a factor of two from the experimental results, a limit which was suggested as a reasonable expectation for a crude model of the type employed. Indeed the agreement is very much better than a factor of 2.

Figures 8-11 present comparisons of the hybrid model with the experimental spectra of this work. A result using average hierarchy lifetimes with nucleon mean free paths multiplied by a factor of four (the parameter found

necessary by other workers using this approach<sup>22)</sup>) are also shown. Both approaches give nearly identical results for all systems, but it is felt that the long mean free paths required when using average hierarchy lifetimes are unrealistic and the consequence of improper bookkeeping<sup>23)</sup>. The calculations of figs. 8-11 do not reproduce the experimental cross sections, giving larger errors at larger neutron energies. This illustrates the importance of considering the role of the direct-reaction term due to surface interactions as given by the first term of eq. (8) for nucleon-induced reactions.

### 5. Conclusions

Comparisons in this work between calculated and experimental ( $p,n$ ) spectra imply the following: (1) the geometry-dependent hybrid model is quite adequate in predicting the absolute cross sections and shapes of continuum ( $p,n$ ) spectra in the 25-45 MeV bombarding energy region, as well as in the 18-26 MeV region investigated by Grimes et al.<sup>2)</sup>, (2) the spectra are reproduced nearly equally well at all projectile energies and for all target masses included in this survey, (3) the parameters used in these calculations are the same as those used for ( $p,p'$ ) spectra, showing a consistency for the model independent of exit channel, and (4) the main discrepancy in these results is an underestimation of calculated neutron yields around 20 MeV for some of the spectra. Results of this work suggest that claims that agreement of calculated ( $p,p'$ ) spectra with experimental results is fortuitous may well be in error. Claims that ( $p,n$ ) calculations with the GDH model fail to give good agreement with experimental results are inconsistent with the observations of this work.

### References

1. M. Blann, Ann. Rev. Nucl. Sci. 25 (1975).
2. S.M. Grimes, J.D. Anderson, J.C. Davis and C. Wong, Phys. Rev. C8 (1973) 1770.
3. E. Gadioli and E. Gadioli-Erba, Acta. Phys. Slovaca (1975) to be published; private communication.

4. R.A. Vinyard, J.E. Lutkin, and G.W. McBeth, Nucl. Instr. Meth. 95(1971)141.
5. E.C. Booth and B.S. Madsen, Nucl. Phys. A206(1973)293.
6. R.R. Doering, D.M. Patterson and Aaron Galonsky, Phys. Rev. C 12(1975).
7. R. Kurz, University of California Report UCRL-11339, unpublished (1964); S.T. Thornton and J.R. Smith, Nucl. Instr. Meth. 96(1971)551.
8. R.R. Doering, Ph.D. Thesis, Michigan State University, unpublished (1974).
9. R. St. Onge, Aaron Galonsky, T.M. Amos, and R.K. Jolly, Nucl. Instr. Meth. 126(1975).
10. J.J. Griffin, Phys. Rev. Letts. 17(1966)478.
11. T. Ericson, Adv. Phys. 9(1960)423.
12. F.C. Williams, Jr., Phys. Lett. 31B(1970)184.
13. M. Blann, "Preequilibrium Models for Nuclear Reactions", Proceedings of the Summer School in Nuclear Physics, Predsal, Romania, Sept. 1974 (in press); Report C00-3494-13.
14. K. Kikuchi and M. Kawai, "Nuclear Matter and Nuclear Interactions", North Holland Publishing Co., Amsterdam (1968).
15. M.L. Goldberger, Phys. Rev. 74(1948)1268.
16. M. Blann, Phys. Rev. Lett. 27(1971)337; 700E; 1550E.
17. M. Blann, Nucl. Phys. A213(1973)570.
18. F.D. Beccetti and G.W. Greenlees, Phys. Rev. 183(1969)1190.

## Figure Captions

**Fig. 1-(a-d):** Neutron ( $n$ ) and gamma-ray ( $\gamma$ ) TOF spectra at  $10^\circ$  for  $E_p = 45$  MeV. Each channel represents 0.1 nsec.

**(e-f):** The corresponding differential cross sections per unit solid angle and per unit neutron energy interval. The bin width is 0.1 MeV, and the resolution is about  $1-1/2$  MeV at  $E_n = 45$  MeV.

**Fig. 2:** Experimental and calculated  $^{54}\text{Fe}(p,p')$  spectra. Experimental angle-integrated spectra (heavy solid line) are from F.E. Bertrand and R.W. Peelle, Phys. Rev. C8 (1973) 1045.

Calculated results are from the GDH model using intranuclear transition rates based on the imaginary optical potential (dot-dash curve) and nucleon-nucleon scattering (thin solid curve). Average nuclear densities were used in these calculations; no equilibrium components have been added to calculated results. The error bar represents  $\pm 20\%$  and is shown to give a measure of the agreement between calculated and experimental results.

**Fig. 3:** Experimental and calculated  $^{209}\text{Bi}(p,p')$  spectra. Experimental and calculated results are as in Fig. 2, except that an equilibrium component (dotted curve) has been included in the calculated spectrum based on nucleon-nucleon scattering intranuclear transition rates at  $E_p = 62$  MeV. Additional dashed curves have been added to indicate the direct-reaction term (higher-energy dashed curve) and the sum of all higher order terms.

**Fig. 4:** Experimental and calculated  $^{48}\text{Ca}(p,n)$  spectra at 25, 35, and 45 MeV incident proton energy. The solid curve with structure represents the experimental result. The steep dot-dash curve represents the pure equilibrium component (calculated). The dotted curve in the 45-MeV spectrum represents the calculated second-chance preequilibrium component using the hybrid model. The smooth solid curve represents the equilibrium-plus-preequilibrium (GDH) calculation in which  $\lambda_+(\epsilon)$  was calculated using the imaginary optical potential averaged along the particle trajectory or over the nuclear radius. The dashed curve is the corresponding result for which  $\lambda_+(\epsilon)$  is based on nucleon-nucleon scattering cross sections. The dot-dash curve

which is near to the other preequilibrium results is the sum of equilibrium and pre-equilibrium calculations, for which the latter used  $\lambda_+(\epsilon)$  for N-N scattering evaluated for the maximum density along the incident particle trajectory. A  $\pm 20\%$  error bar has been included to help compare the degree of agreement between theoretical and experimental results.

**Fig. 5:** Experimental and calculated  $^{90}\text{Zr}(\text{p},\text{n})$  spectra.  
Curves have the same significance as in fig. 4.

**Fig. 6:** Experimental and calculated  $^{120}\text{Sn}(\text{p},\text{n})$  spectra.  
Curves have the same significance as in fig. 4.

**Fig. 7:** Experimental and calculated  $^{208}\text{Pb}(\text{p},\text{n})$  spectra.  
Curves have the same significance as in fig. 4.

**Fig. 8:** Experimental and calculated  $^{48}\text{Ca}(\text{p},\text{n})$  spectra.  
The thin solid curve represents the result of the hybrid-model calculation (eq. 5) using  $\lambda_+(\epsilon)$  based on N-N scattering cross sections. The dashed curve represents a similar calculation in which the average lifetime due to intranuclear transitions of each hierarchy in the equilibration sequence is calculated from N-N scattering cross sections. The latter lifetimes were arbitrarily increased by a factor of 4.

**Fig. 9:** Experimental and calculated  $^{90}\text{Zr}(\text{p},\text{n})$  spectra.  
Curves are as in fig. 8.

**Fig. 10:** Experimental and calculated  $^{120}\text{Sn}(\text{p},\text{n})$  spectra.  
Curves are as in fig. 8.

**Fig. 11:** Experimental and calculated  $^{208}\text{Pb}(\text{p},\text{n})$  spectra.  
Curves are as in fig. 8.

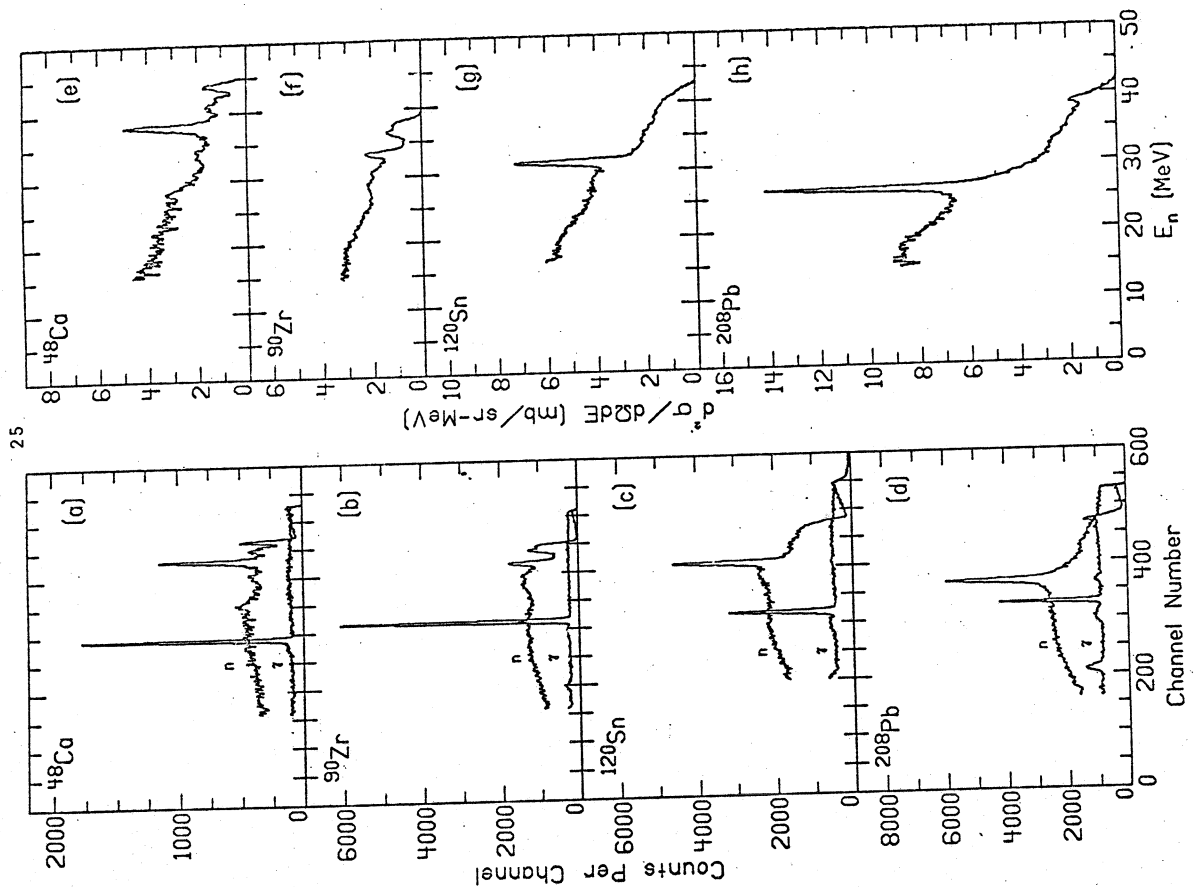


Fig. 1

26

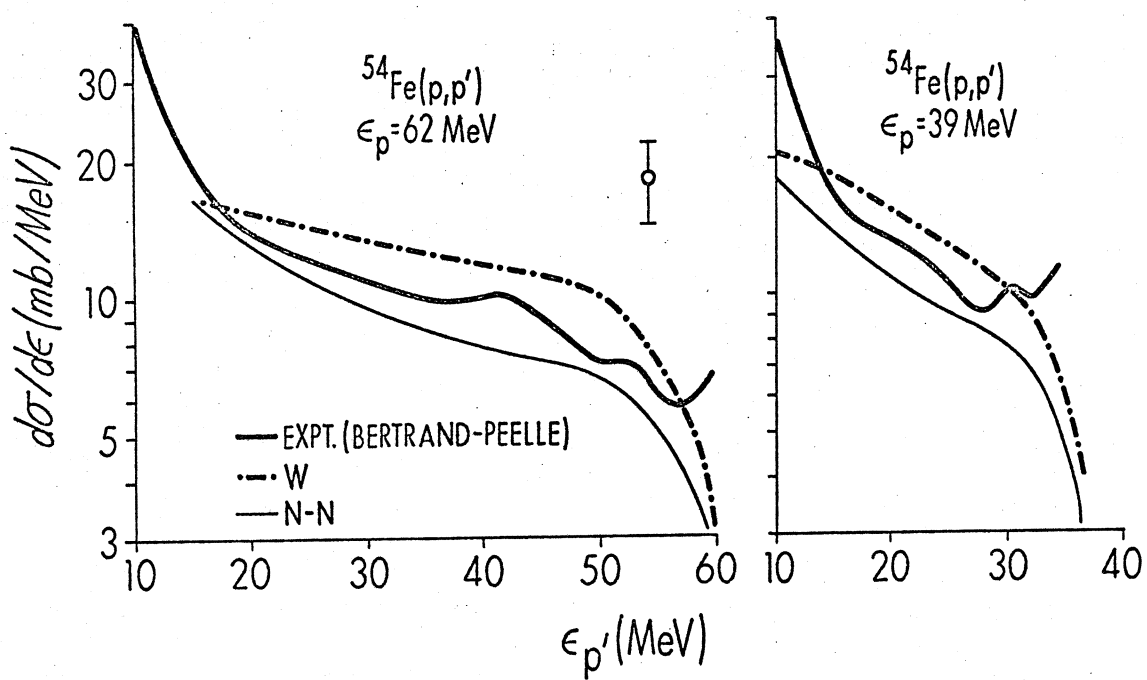


Fig. 2

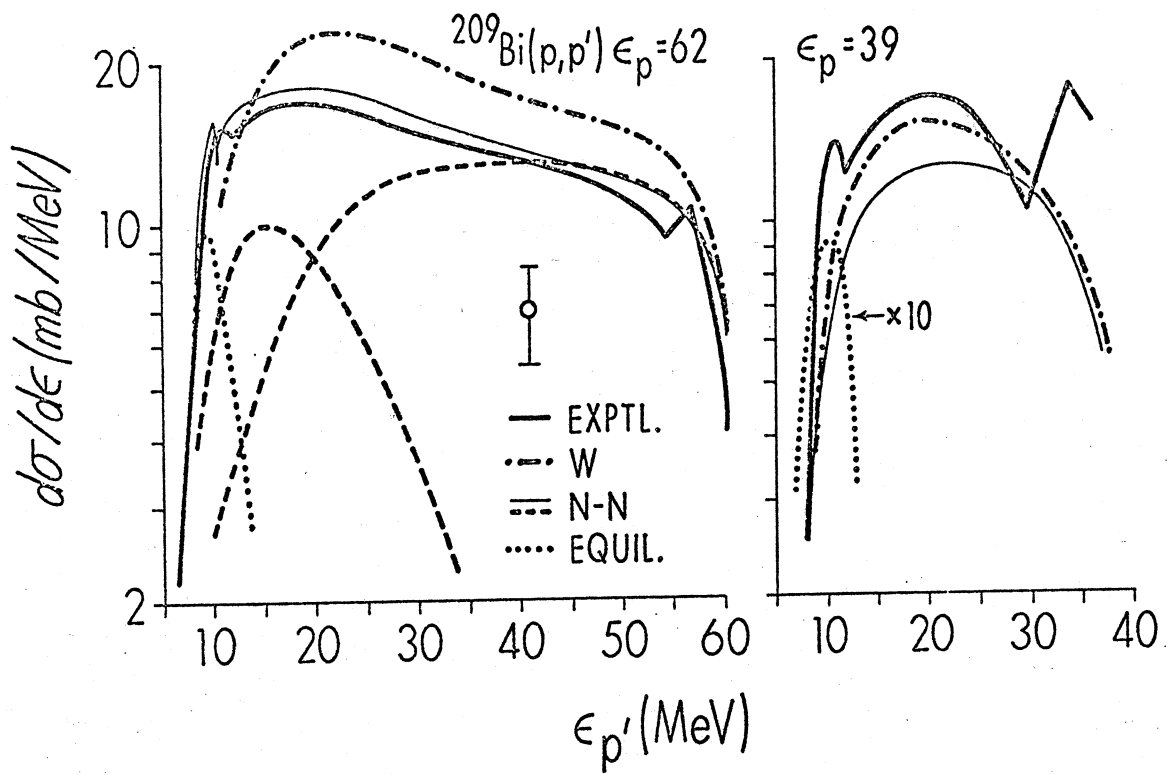


Fig. 3

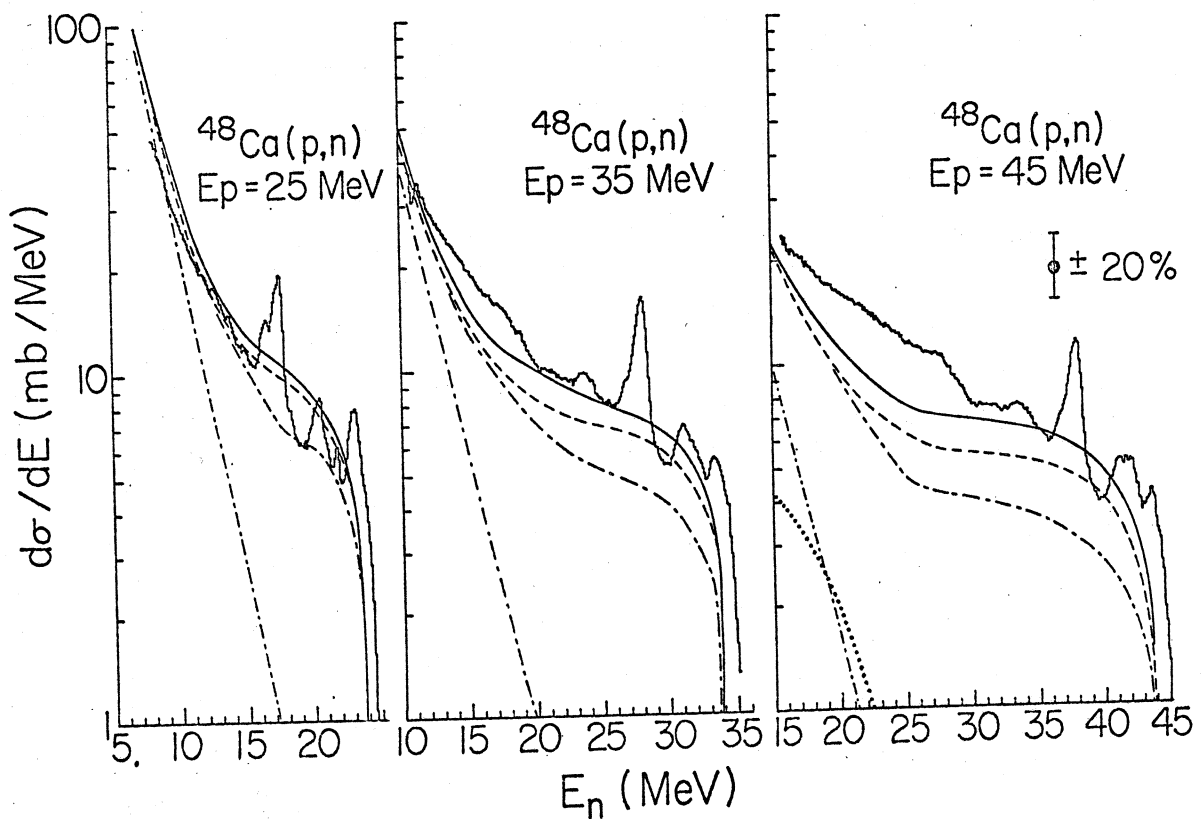


Fig. 4

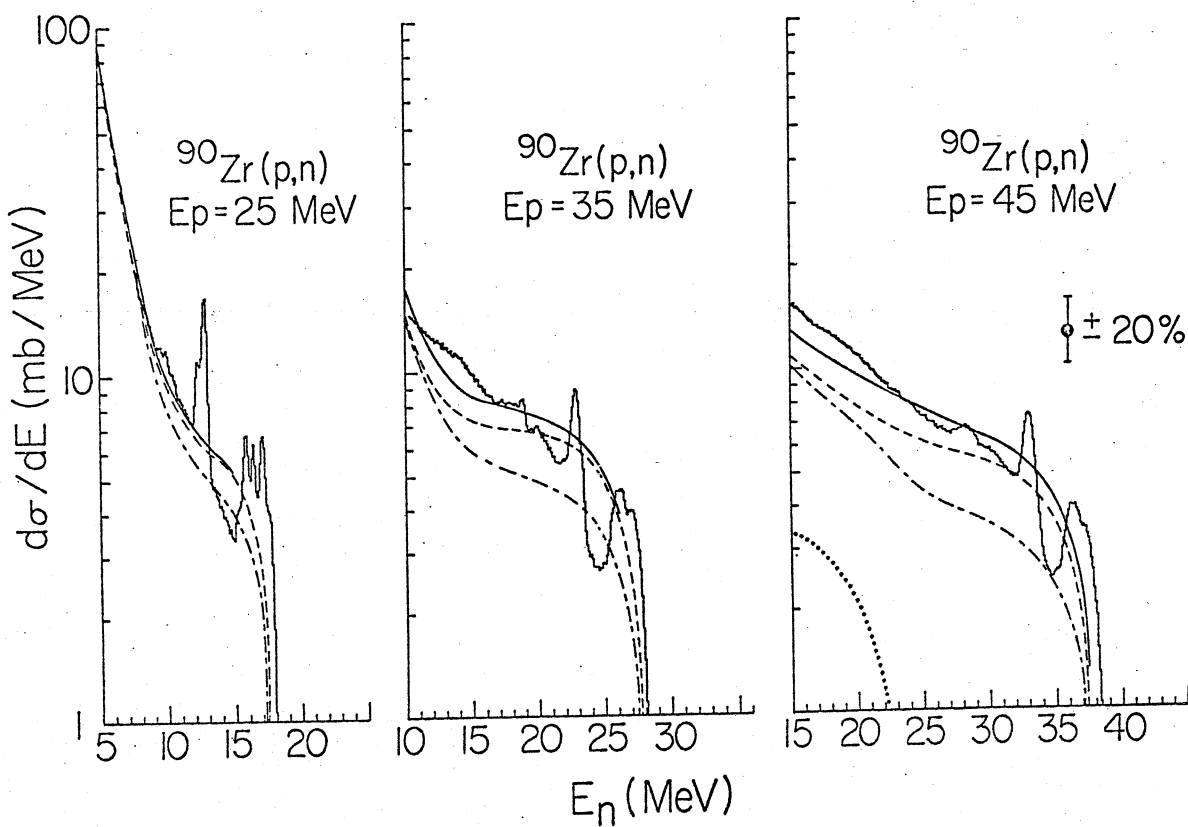


Fig. 5

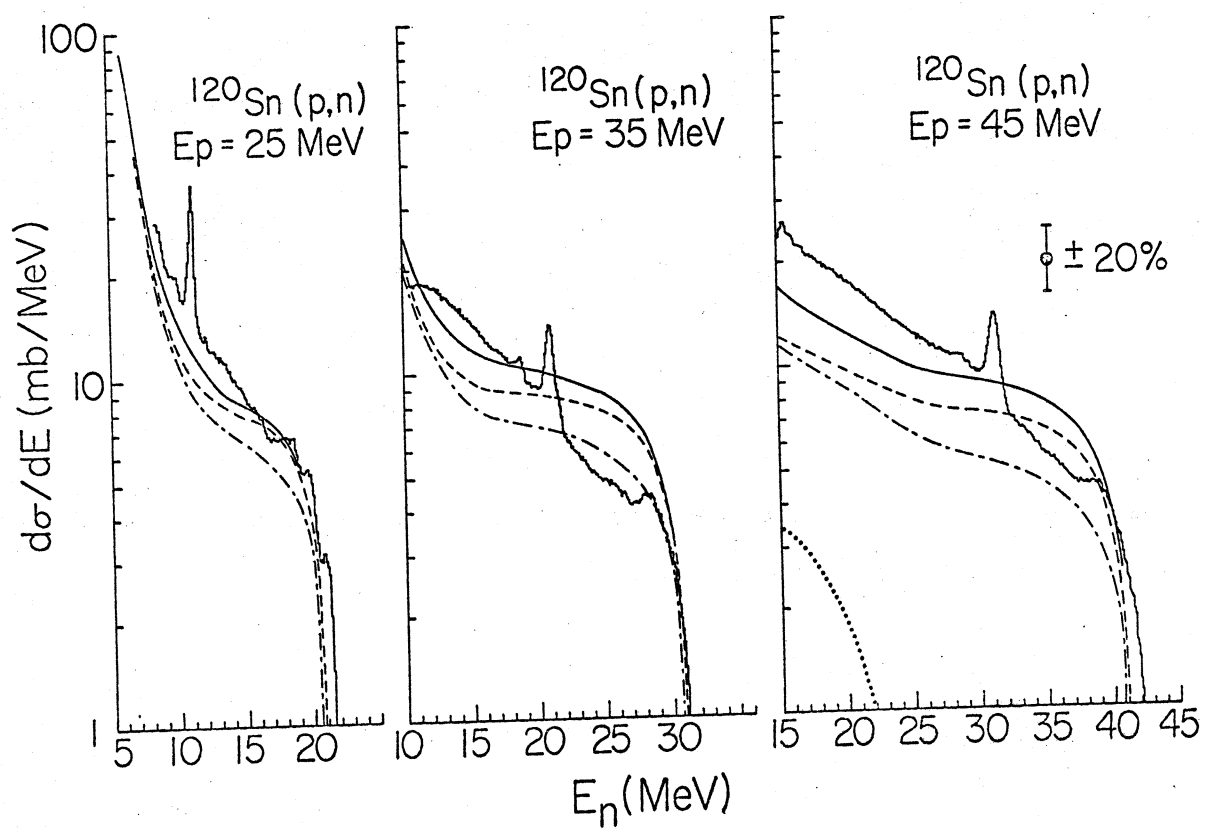


Fig. 6

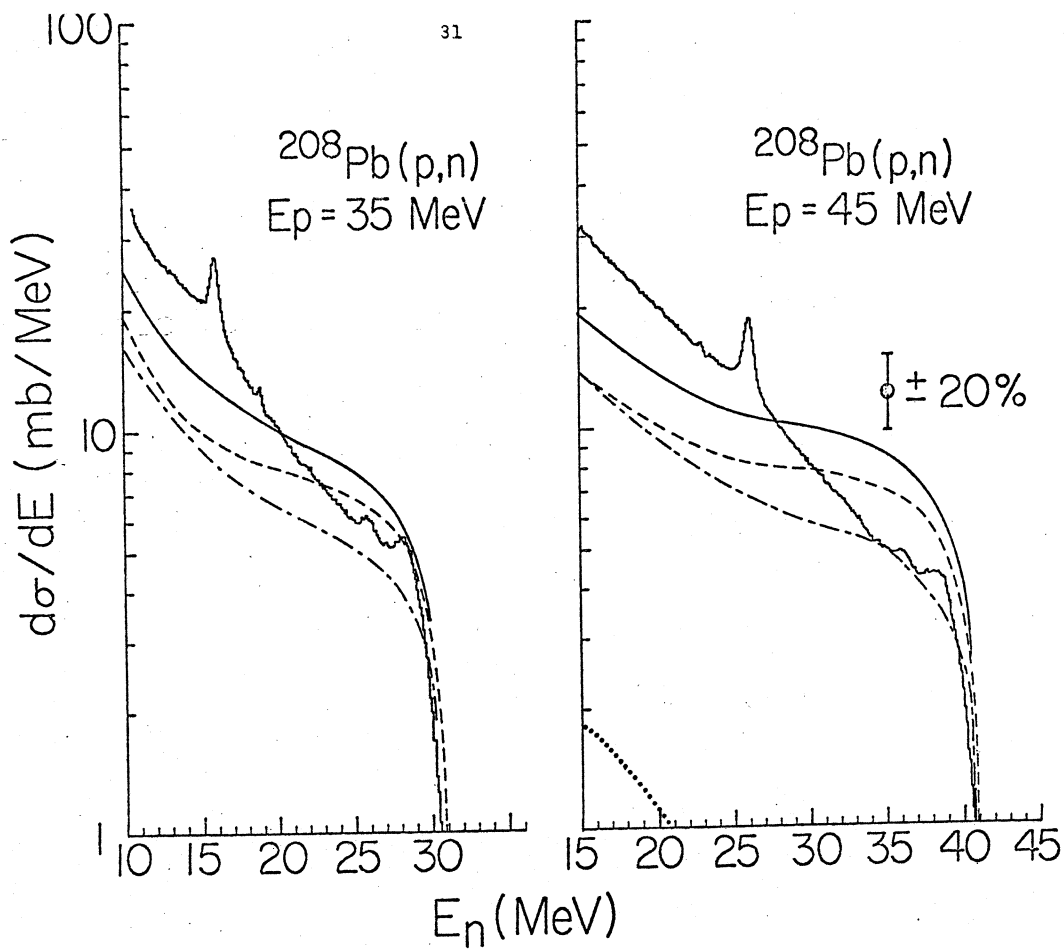


Fig. 7

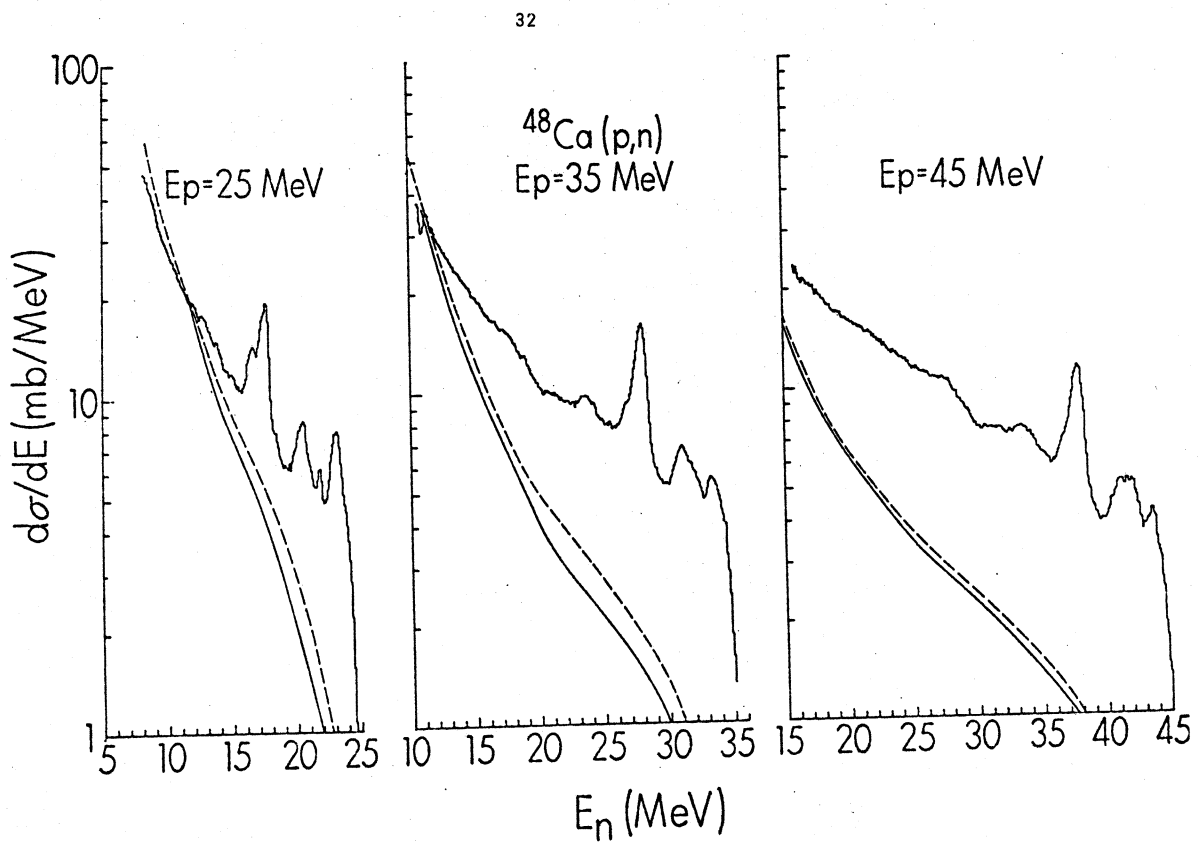


Fig. 8

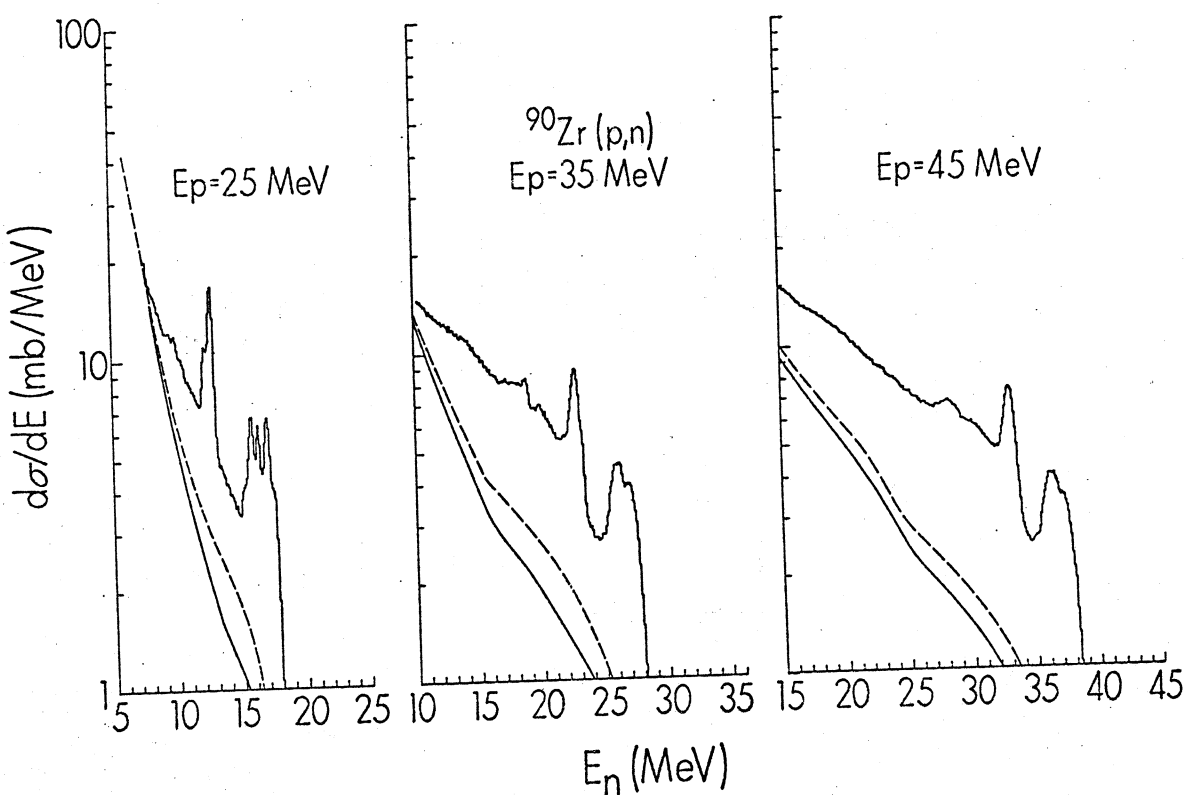


Fig. 9

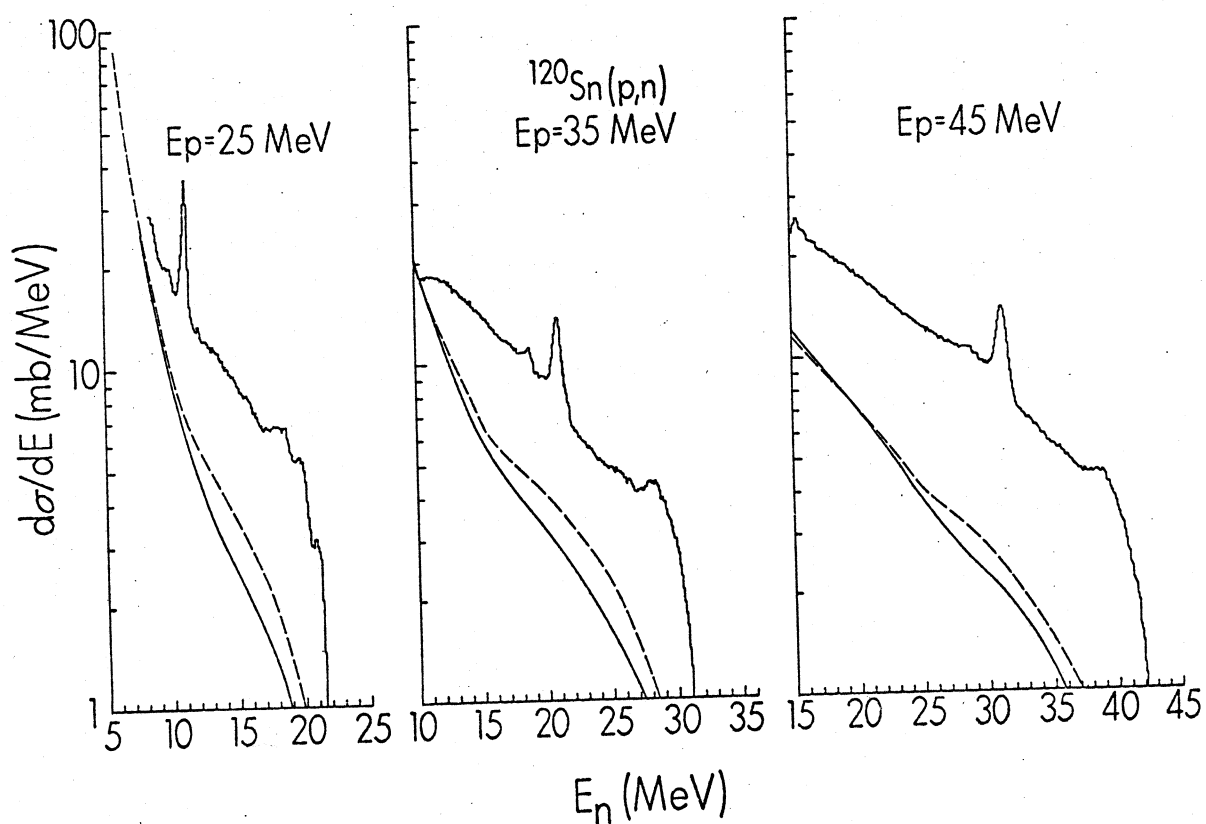


Fig. 10

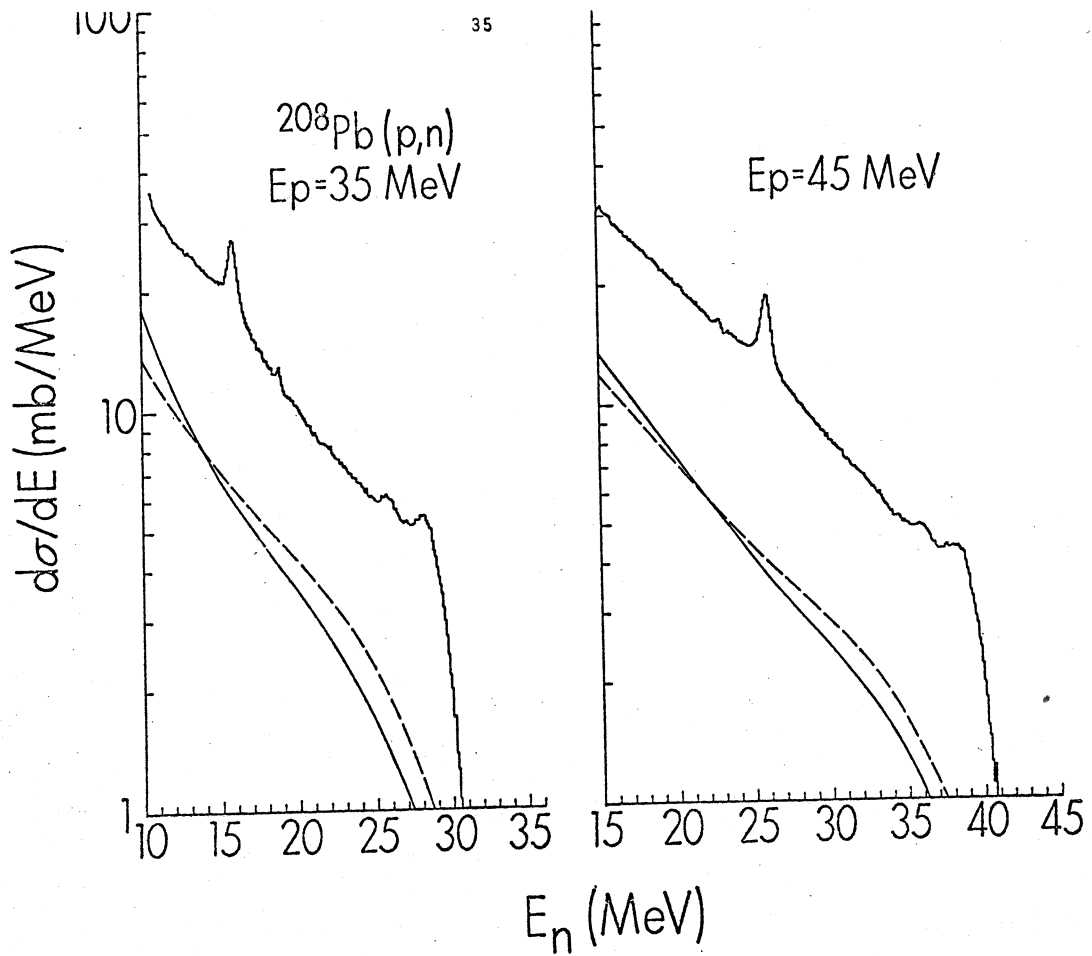


Fig. 11